CHEMISTRY
A EUROPEAN JOURNAL

DOI: 10.1002/chem.200701865

Structural, Magnetic Coupling and Oxidation State Trends in Models of the $CaMn_4$ Cluster in Photosystem II

Simon Petrie, Rob Stranger,* and Ron J. Pace[a]

Abstract: Density functional theory calculations are reported on a set of isomeric structures **I**, **II** and **III** that share the structural formula $[CaMn_4C_9H_{10}N_2O_{16}]^{q+}\cdot(H_2O)_3$ ($q=-1$, 0, 1, 2, 3). Species **I** has a skeletal structure, which has been previously identified as a close match to the ligated $CaMn_4$ cluster in Photosystem II, as characterized in the most recent 3.0 Å crystal structure. Structures **II** and **III** are rearrangements of **I**, which largely retain that model's bridging ligand framework, but feature metal atom positions broadly consistent with, respectively, the earlier 3.5 and 3.2 Å crystal structures for the Photosystem II water-oxidising complex (WOC). Our study explores the influence of the cluster charge state (and hence *S* state) on several important properties of the model structures; including the relative energies of the three models, their interconversion, trends in the individual Mn oxidation states, preferred hydration sites and favoured modes of magnetic coupling between the manganese atoms. We find that, for several of the explored cluster charge states, modest differences in the bridging-ligand geometry exert a powerful influence over the individual manganese oxidation states, but throughout these states the robustness of the tetrahedron formed by the Ca and three of the Mn atoms remains a significant feature and contrasts with the positional flexibility of the fourth Mn atom. Although structure **I** is lowest in energy for most *S* states, the energy differences between structures for a given *S* state are not large. Overall, structure **II** provides a better match for the EXAFS derived metal–metal distance parameters for the earlier *S* states (S_0 to S_2), but not for S_3 in which a significant structural change is observed experimentally. In this *S* state structure **III** provides a closer fit. The implications of these results, for the possible action of the WOC, are discussed.

Keywords: density functional calculations · EXAFS spectroscopy · metalloproteins · mixed-valent compounds · photosystem II

Introduction

The atomic-level mechanism of water oxidation by Photosystem II (PSII) remains elusive despite intense interdisciplinary scrutiny. One of the difficulties experienced in characterizing this mechanism is in nailing down a specific structure for the water oxidizing complex (WOC), because the laboratory method of choice for metalloprotein structural characterization—single-crystal X-ray crystallography (XRD)—has been shown to yield cluster geometries,[1–5] which are not mutually consistent. Moreover, it has recently been shown that the X-ray fluxes required to obtain usable XRD results are more than sufficient to induce structural degradation in the highly photosensitive region of the metal core and its environs.[6] Consequently, there now appears to be a heightened awareness that structural information on the WOC must necessarily be pieced together from an array of different laboratory approaches. Areas of consensus regarding the WOC include the view that it comprises four Mn and one Ca atom, bridged in some manner and ligated by six or seven amino acid residues within the main peptide sequence of PSII. Areas of contention include the oxidation states on the Mn atoms for any given state S_0 to S_3 (and transient S_4) for the WOC, the nature of the bridging ligands, the sites of "reactant" water ligation and the overall shape of the $CaMn_4$ cluster.

There is considerable scope for quantum chemical approaches to play an important role in the quest to unravel the structure and mechanism of the WOC, this is partially owed to the intractability of the WOC in the face of leading-edge laboratory approaches. The research groups of Siegbahn[7–11] and Batista[12–14] have been intensively involved

[a] S. Petrie, Prof. R. Stranger, R. J. Pace
Chemistry Department, the Faculties, Australian National University
Canberra ACT 0200 (Australia)
Fax: (+61) 2-6125-0760
E-mail: rob.stranger@anu.edu.au

Supporting information for this article is available on the WWW under http://www.chemeurj.org/ or from the author.

WILEY InterScience DISCOVER SOMETHING GREAT
© 2008 Wiley-VCH Verlag GmbH & Co. KGaA, Weinheim

in attempts to theoretically characterize the WOC, through calculations on hydrated, bridged $CaMn_4$ clusters. The most recent published studies of these groups[9,11,13,14] have concerned density functional theory (DFT) calculations on metal clusters with an overall structural similarity to the $CaMn_4$ geometry seen in the 3.2 Å resolution "London" crystal structure of the WOC, reported in 2004.[4] An alternative theoretical model, recently presented by Kusunoki,[15] again uses DFT but explores a $CaMn_4$ geometry derived from the most recent 3.0 Å resolution Berlin WOC crystal structure, reported in 2005.[5] A further commonality between these theoretical studies[8–15] is the implicit assumption, which remains contentious, that the S_0 state of PSII has a WOC oxidation state combination of $(Mn^{III})_3Mn^{IV}$. In order to avoid highly charged clusters in the higher S states, these studies[8–15] require the incorporation of at least five oxo and/or hydroxo bridges between the Mn atoms, an aspect on which the crystal structures reported to date[1–5] remain silent.

Our own recent foray[16] into efforts to characterize the WOC also draws inspiration from the bridging ligand framework revealed by the 3.0 Å resolution Berlin XRD,[5] as we judge that this most recent crystal structure features the Mn coordination geometries that appear the most consistent with common transition metal ligation modes (such as mildly distorted octahedral coordination). However, we have sought so far as possible to minimise the number of structural assumptions made in our modelling, to the extent that "London"-like[4] and "Hyogo"-like[2] metal atom configurations have also been investigated, as has consideration that the $(Mn^{III})_3Mn^{IV}$ oxidation state combination may correspond to either the S_0 or the S_2 state of PSII. Our models differ from those of other groups[8–15] in that they possess fewer oxo bridges between the Mn atoms, which has the effect of stabilizing lower Mn oxidation states. One startling result of our initial calculations on $[CaMn_4C_9H_{10}N_2O_{16}]^+ \cdot(H_2O)_n$ ($n=0$–7), reported in our recent work,[16] was that each of the three most recently reported (and highest resolution) XRD structures[2,4,5] showed metal positions that were broadly consistent with isomeric $[CaMn_4C_9H_{10}N_2O_{16}]^+ \cdot(H_2O)_n$ structures between which interconversion appeared reasonably facile. This result admits the somewhat disconcerting possibility[16] that structural rearrangement of the isolated WOC may be occurring *before*, rather than *during*, the X-ray irradiation of single crystals.

As a continuation of our study into possible models of the WOC, here we subject the structural isomers **I**·$(H_2O)_3$, **II**·$(H_2O)_3$ and **III**·$(H_2O)_3$, respectively, featuring metal atom positions consistent with the Berlin,[5] Hyogo,[2] and London[4] XRD structures, to greater scrutiny; canvassing five overall ionization levels and all feasible high-spin single-determinant magnetic coupling patterns for the four constituent high-spin Mn atoms. The specification of three explicit water ligands for each structure is intended to ensure that each metal atom is able to achieve coordinative saturation. Although a total of three or more water molecules may or may not be sufficient to drive water oxidation (a mechanistic detail that is beyond the scope of the present work), our experience with varying hydration levels on these models has been that the grossest structural distortion tends to occur in structures with two or fewer H_2O ligands. Thus three water ligands provide for a reasonably stable complex, in the sense that addition of any further, relatively weakly bound, H_2O ligands is expected to result in only very minor changes to the intermetallic distances (and hence to the magnetic interactions between Mn atoms, which are sensitive to metal–metal distances among other considerations). Furthermore, recent electron spin-echo envelope modulation (ESEEM) studies of the interaction between substrate water molecules and the WOC site, during functional turnover, identify a minimum of 3 water molecules in magnetic contact with the manganese cluster in the S_0 and S_1 states.[17]

The focus of our calculations reported here is an attempt to unravel the interrelationship between charge state, geometric structure, magnetic coupling modes, Mn oxidation states and preferred water binding sites. These calculations are intended as a platform from which subsequent exploration of the mechanism of water oxidation by PSII can be undertaken.

Results and Discussion

In the discussion which follows, we examine in detail the principal results of extensive calculations on the trihydrated $CaMn_4$ cluster models, before appraising their relevance to the growing body of experimental results on the structure and mechanism of the PSII water oxidizing complex.

Overview of geometric trends: The structures for the lowest-energy trihydrated complexes of doubly-charged type **I** (Berlin), **II** (Hyogo) and **III** (London) complexes are displayed in Figure 1. This Figure also shows, for comparison, the metal atom positions reported in the three most recent XRD studies.

Further details of the optimized geometries, in each explored charge state, are summarised in Tables 1 and 2. Table 1 presents a detailed listing of metal–metal distances (and related angles and dihedrals) within the complexes. The geometries summarised here are those optimised for the consistently antiferromagnetic ABAB coupling pattern described in the Theoretical Methods section, in the oxidation-state pattern identified by initial optimizations on ferromagnetically coupled structures.[18] Within a given oxidation-state pattern the variation between differently coupled optimized geometries is generally small. More dramatic geometric differences can arise if antiferromagnetically coupled structures have an oxidation-state pattern that differs from that dictated by ferromagnetic coupling, as is the case for example for $\mathbf{II}^{1-}$ and $\mathbf{III}^{2+}$ (discussed subsequently within the text). The geometry relevant to the ferromagnetically coupled oxidation-state pattern, as shown in Table 1 is, however, likely to be more useful as a comparison with experi-

 © 2008 Wiley-VCH Verlag GmbH & Co. KGaA, Weinheim

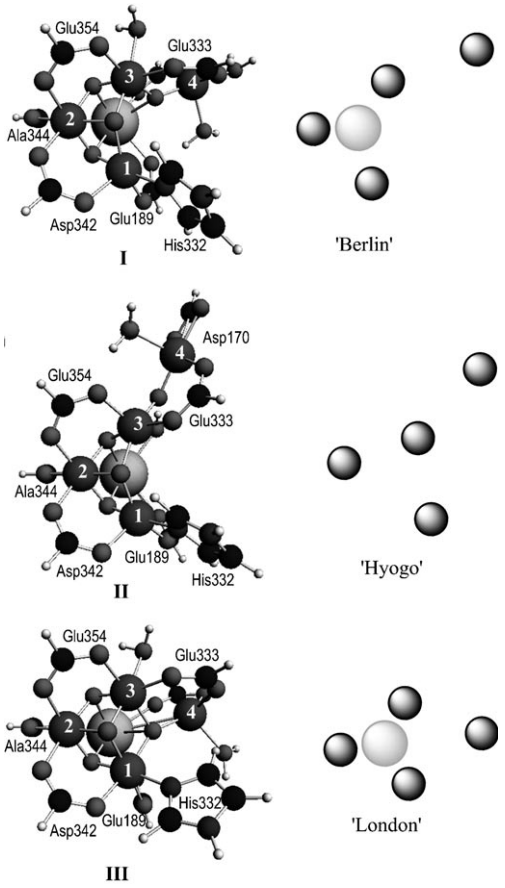

Figure 1. Optimized geometries of tri-hydrated **I**, **II** and **III** in the +2 charge state, obtained at the BP/TZP level of theory. Mn atoms 1 to 4 are numbered to indicate the notation used throughout this work, although to aid in comparison with the various experimental results, we have shown also (to the right hand side of each optimized geometry) the XRD-derived metal atom positions from the most closely related crystal structure. The amino acid residues labelled are consistent with the connectivity assigned in the Berlin crystal structure. Although this connectivity differs in detail with that obtained in the earlier Hyogo and London studies, we have mapped the Berlin protein ligation in **I** onto structures **II** and **III** with assumed retention of the amino acid identities. Note that for structures **I** and **III**, the chosen projection obscures the Asp170 residue, which lies behind the Glu333 in this orientation.

mental structural data obtained from flash turnover conducted at, or near, room temperature. Table 2 gives an overview of the range of values encountered for each of the geometric parameters within each structure type. (Note that the Table 2 values encompass not only the trihydrated complexes, but also the values found for hydration ranging from zero to seven water molecules.)

Table 2. Observed range of values for Mn–Mn and Ca–Mn bond lengths and angles in the $CaMn_4$-containing model complexes **I**, **II** and **III**.

Parameter[a]	**I**	**II**	**III**
r(Mn(1)–Mn(2))	2.7–2.9	2.6–2.9	2.6–2.9
r(Mn(2)–Mn(3))	2.7–2.9	2.7–2.9	2.6–2.9
r(Mn(1)–Mn(3))	3.1–3.5	3.2–3.7	2.8–3.1
r(Mn(3)–Mn(4))	2.7–3.4	3.2–3.3	3.1–3.5
r(Mn(1)–Mn(4))	4.2–5.5	6.1–6.8	3.5–3.8
∠(Mn[123])	70–79	71–85	62–68
∠(Mn[234])	123–137	148–156	114–124
∠(Mn[134])	81–125	130–160	64–77
∠(Mn[1234])	42–111	104–173	24–48
r(Ca–Mn(1))	3.3–3.7	3.4–4.0	3.2–3.7
r(Ca–Mn(2))	3.1–3.3	2.9–3.5	3.1–3.4
r(Ca–Mn(3))	3.1–3.5	3.5–4.2	3.3–3.8
r(Ca–Mn(4))	3.3–3.9	5.1–6.4	3.4–4.6
∠(CaMn[12])	58–62	55–61	62–67
∠(CaMn[123])	67–74	76–87	74–81

[a] Bond lengths in [Å] and bond angles and dihedrals [°].

Several geometric trends are apparent from the data within Table 1. First, within each structure type (**I**, **II** or **III**) many of the intermetallic parameters do not vary widely: for example, the Mn(1)–Mn(2) distance changes by less that 0.15 Å in structure **II** across the charge range $q=-1$ to $+3$ and the variation in the Mn(2)–Mn(3) distance across this range is even narrower. Second, across different structure types there are also several parameters, which do not change greatly: The Mn(1)–Mn(2) and Mn(2)–Mn(3) distances are examples, differing by less than 0.2 Å across all surveyed structures. In fact, the near-constancy of so many of the geometric parameters, independent of charge state and structure type, echoes and amplifies a point first noted

Table 1. Influence of charge state on Mn–Mn and Ca–Mn bond lengths and angles in the trihydrated $CaMn_4$-containing model complexes **I**, **II** and **III**.

Parameter[a]	$\mathbf{I}^{-1}$	$\mathbf{I}^{0}$	$\mathbf{I}^{+1}$	$\mathbf{I}^{+2}$	$\mathbf{I}^{+3}$	$\mathbf{II}^{-1}$	$\mathbf{II}^{0}$	$\mathbf{II}^{1}$	$\mathbf{II}^{2}$	$\mathbf{II}^{3}$	$\mathbf{III}^{-1}$	$\mathbf{III}^{0}$	$\mathbf{III}^{+1}$	$\mathbf{III}^{+2}$	$\mathbf{III}^{+3}$
r(Mn(1)–Mn(2))	2.873	2.737	2.747	2.794	2.831	2.832	2.701	2.739	2.738	2.756	2.728	2.738	2.686	2.775	2.791
r(Mn(2)–Mn(3))	2.838	2.818	2.785	2.764	2.789	2.749	2.776	2.750	2.765	2.778	2.807	2.855	2.720	2.688	2.719
r(Mn(1)–Mn(3))	3.341	3.481	3.422	3.427	3.352	3.683	3.480	3.400	3.428	3.477	3.197	3.235	2.928	2.872	2.968
r(Mn(3)–Mn(4))	2.798	2.928	3.334	3.290	3.083	3.239	3.173	3.215	3.226	3.286	3.092	3.241	3.372	3.229	3.204
r(Mn(1)–Mn(4))	5.341	5.380	4.934	4.886	5.088	6.695	6.414	6.404	6.386	6.625	4.622	4.169	3.627	3.744	3.710
∠(Mn[123])	71.6	77.6	76.5	76.2	73.2	82.6	78.9	76.5	77.1	77.8	70.5	70.6	65.6	63.4	65.2
∠(Mn[234])	123.5	131.0	129.8	129.1	138.0	152.9	154.1	153.7	153.5	151.7	127.4	125.7	116.0	121.0	119.4
∠(Mn[134])	120.6	113.9	93.8	93.3	104.4	150.6	149.2	151.0	147.3	156.8	94.6	80.1	69.9	75.4	73.8
∠(Mn[1234])	106.3	88.5	56.2	57.8	69.7	148.2	146.0	156.1	143.7	170.7	64.0	36.3	38.8	46.5	44.1
r(Ca–Mn(1))	3.381	3.414	3.507	3.534	3.668	3.656	3.550	3.602	3.744	3.809	3.320	3.302	3.431	3.426	3.474
r(Ca–Mn(2))	3.172	3.179	3.181	3.217	3.271	3.117	3.214	3.227	3.283	3.256	3.243	3.120	3.298	3.311	3.379
r(Ca–Mn(3))	3.189	3.220	3.289	3.353	3.450	3.631	3.698	3.690	3.846	4.011	3.298	3.264	3.507	3.582	3.670
r(Ca–Mn(4))	3.354	3.500	3.788	3.740	4.041	5.689	5.679	5.801	5.788	6.394	3.405	3.915	3.649	3.647	3.656
∠(CaMn[12])	60.3	61.1	59.7	59.8	58.8	55.7	60.1	59.4	58.4	56.8	64.0	61.4	63.9	63.5	64.2
∠(CaMn[123])	−68.5	−67.2	−69.4	−70.7	−72.4	−77.6	−78.4	−78.9	−81.1	−85.2	−71.0	−71.2	−77.4	−80.8	−81.0

[a] Bond lengths in [Å] and bond angles and dihedrals [°].

© 2008 Wiley-VCH Verlag GmbH & Co. KGaA, Weinheim

Table 3. Influence of charge state q on computed total bond energies and Mn atom spin densities in the trihydrated $CaMn_4$-containing model complexes **I**, **II** and **III**.

		S_{max} (AAAA)					BS (ABAB)				
	q	E_{bond}/E_h[a]	$\mu_{spin}(1)$[b]	$\mu_{spin}(2)$[b]	$\mu_{spin}(3)$[b]	$\mu_{spin}(4)$[b]	E_{bond}/E_h[a]	$\mu_{spin}(1)$[b]	$\mu_{spin}(2)$[b]	$\mu_{spin}(3)$[b]	$\mu_{spin}(4)$[b]
I	−1	−12.30300	3.84	3.87	3.78	4.78	−12.31280	−3.79	3.74	−3.56	4.64
I	0	−12.22626	3.85	2.87	3.85	4.79	−12.23713	3.79	−2.74	3.63	−4.67
I	+1	−12.00884	3.85	2.89	3.75	3.92	−12.01585	3.80	−2.75	3.68	−3.74
I	+2	−11.67491	3.80	2.86	2.97	3.85	−11.67842	3.77	−2.78	2.82	−3.79
I	+3	−11.19738	2.93	2.84	2.88	3.86	−11.19993	−2.90	2.77	−2.74	3.81
II	−1	−12.29292	4.76	2.84	3.89	4.82	−12.30818	4.55	−2.62	3.76	−4.73
II	0	−12.20499	3.82	2.90	3.86	4.80	−12.21891	3.77	−2.75	3.59	−4.69
II	+1	−12.00735	3.83	2.91	3.82	3.89	−12.01440	3.78	−2.76	3.68	−3.77
II	+2	−11.65806	3.44	2.87	3.32	3.90	−11.66418	3.36	−2.76	3.18	−3.80
II	+3	−11.18388	3.00	2.88	3.75	2.79	−11.19400	3.04	−2.77	3.44	−2.58
III	−1	−12.28731	3.83	2.86	4.77	4.83	−12.30647	3.79	−2.48	4.42	−4.74
III	0	−12.21435	3.84	2.87	3.87	4.80	−12.22400	3.79	−2.73	3.61	−4.71
III	+1	−12.00061	3.01	2.86	3.84	4.71	−12.00035	−2.70	2.80	−3.68	4.69
III	+2	−11.66269	3.13	2.83	2.93	4.60	−11.66233	−2.77	2.83	−2.68	4.62
III	+3	−11.20386	2.89	2.81	2.83	3.91	−11.20146	−2.81	2.81	−2.79	3.88

[a] Bond energy, in Hartrees, of the indicated structure. [b] Mn atom spin density for the indicated structure.

in our previous report on monopositively charged PSII WOC models.[16] The tetrahedron described by Mn(1), Mn(2), Mn(3) and Ca is an extremely robust structural motif and appears highly resistant to distortion or fragmentation. The variation between structures **I**, **II** and **III**, whatever the charge state, can be described almost entirely in terms of the orientation of the Mn(4)-containing side-arm relative to the calcium trimanganese core of the complexes. Consequently, the principal geometric variability is seen in parameters such as the Mn(1)–Mn(4) and Ca–Mn(4) distances, the Mn(1)–Mn(3)–Mn(4) angle and the Mn(1)-Mn(2)-Mn(3)-Mn(4) dihedral. In fact, the Mn(1)–Mn(4) distance and Mn(1)–Mn(3)–Mn(4) angle comprise the most useful diagnostic for distinguishing a structure as type **I**, **II** or **III**.

Although, in a general sense the structure **I**, **II** or **III** is conserved on repeated oxidation (see the following subsections), there are some charge-state-dependent trends in geometric properties that are evident. For all three model structures, there is a systematic (though not entirely regular) tendency for an increase in the distance between Ca and any of the four Mn atoms, as the charge state increases. This can be attributed to the increasing Coulombic repulsion between the covalently bridged Mn_4 cluster and the electrostatically bound Ca^{2+} ion, although there is no direct influence between the oxidation number on any individual Mn and its distance to Ca, indeed, the Ca–Mn distance is almost universally shortest for Mn(2), which in most charge states is the most highly oxidised manganese atom.

Also evident, for both **I** and **III** (but not for **II**) are trends towards elongation of Mn(3)–Mn(4) and contraction of both Mn(2)–Mn(3) and Mn(1)–Mn(4) as the charge state increases from $q=-1$ to $+3$. As with the Ca–Mn distances detailed above, these trends do not appear directly connected to the oxidation states of the Mn atoms concerned, but relate to the increasing overall charge state of the model complex.

Relative energies as a function of charge state: The calculations also provide useful insights into the relative energies of isomeric clusters (see Table 3), although some caution should be used in interpreting the energetic values. Although we have performed calculations across a range of hydration levels, we have not sought to include any treatment of the encapsulating protein environment, which will certainly have some energetic influence and may well favour one structural motif over another. Similarly, caution must be exercised in examining the energies of different charge states, since our calculations deal exclusively with (hydrated) "vacuum-phase" species and do not consider the broader solvent corrections, which are expected to be necessary to address the appropriate dielectric constant of the protein environment. Within these considerations, it is possible to say that the Berlin-like structure **I** is energetically preferred over **II** and **III** for the -1, 0, $+1$ and $+2$ states whereas the London-like structure **III** displays greater apparent stability than **I** or **II** for the $+3$ state, although the difference in energy between all three structures is never more that 55 kJ mol^{-1} for any given charge state (and is often very much less than that). It is not at all clear that such a comparatively narrow energy range is sufficient to preclude consideration of any of these structures at any charge state, since the models we use feature an abrupt and minimalistic truncation of the extensive protein environment surrounding the WOC active site.

Charge-state-dependent interconversion of structures I and III: Another structural detail reported in our earlier work concerned the close interrelationship between structures **I**,

 © 2008 Wiley-VCH Verlag GmbH & Co. KGaA, Weinheim

II and **III**, as evidenced by the occurrence of interconversion between **I** and **II**, or between **I** and **III**, under some circumstances in the +1 charge state. In fact we can now assert that, at least with regard to structures **I** and **III**, the +1 charge state is rather resistant to interconversion. A greater facility for conversion of structure **III** to **I** is evident for the −1 and 0 charge states, to the extent that geometry optimization of **III** in the neutral charge state is difficult to undertake without accompanying collapse to structure **I**. Similarly, it has proven very difficult to isolate structure **I** in the +3 oxidation state since this structural motif prefers to collapse to the lower-energy structure **III** in this charge state. One rationalisation for this apparent variation in ease of interconversion may lie in the differences in individual Mn atom oxidation states as a function of both charge state and cluster structure (see Table 4). The Mn atom oxidation states, as determined by atomic spin densities on the various Mn atoms, differ in detail between structures **I** and **III** for the −1, +1 and +2 overall charge states, but they are consistent between **I** and **III** in each of the 0 and +3 charge states and this consistency may well facilitate collapse of the higher-energy form ($\mathbf{III}^{0}$, $\mathbf{I}^{+3}$) to the lower-energy form ($\mathbf{I}^{0}$, $\mathbf{III}^{+3}$) within the 0 and +3 charge states.

Table 4. Summary of Mn atom oxidation states (for Mn atoms 1–4) in the explored charge states of the trihydrated $CaMn_4$-containing model complexes **I**, **II** and **III**.

q	S state assignment	**I**	**II**	**III**
−1	S_0 ?	3/3/3/2	2/4/3/2[c]	3/4/2/2[c]
0	S_1 ?	3/4/3/2	3/4/3/2	3/4/3/2
+1	S_0 or S_2	3/4/3/3[a]	3/4/3/3	4/4/3/2
+2	S_1 or S_3	3/4/4/3[b]	$3^{1}/_{2}/4/3^{1}/_{2}/3$[d]	4/4/4/2[e]
+3	S_2 or S_4	4/4/4/3	4/4/3/4	4/4/4/3

[a] An alternative pattern of oxidation states, 3/4/4/2, is also evident for this charge state of structure **I**, but is energetically disfavoured by $\approx 40\ kJ\,mol^{-1}$ for the trihydrated species. [b] An alternative pattern of oxidation states, 4/4/3/3, is also evident for this charge state of structure **I**, but is energetically disfavoured by $\approx 35\ kJ\,mol^{-1}$ for the trihydrated species. [c] This is the pattern delivered by optimisation of the ferromagnetically coupled structure. The lowest-energy coupling mode is, however, found from antiferromagnetically coupled calculations on a 3/3/3/2 oxidation-state pattern. [d] Two competing oxidation-state patterns, 4/4/3/3 and 3/4/4/3, appear almost isoenergetic for this charge state of trihydrated structure **II**. [e] This is the pattern delivered by optimisation of the ferromagnetically coupled structure. The lowest-energy coupling mode is, however, found from antiferromagnetically coupled calculations on a 3/4/4/3 oxidation-state pattern.

The nature of the **I**⇄**III** interconversion may also yield some insight into the oxidation state differences that exist between these two structures. The Berlin-like structure **I** has a bridging connectivity, excluding waters of hydration, that dictates 5 donor atoms for Mn(1), 6 for Mn(2), 5 for Mn(3) and 3 or 4 for Mn(4). The variability of the ligand donor atom count for Mn(4) acknowledges that the non-bridging carboxylate ligand (Asp170) may coordinate in either a monodentate or a bidentate fashion with this Mn atom. The London-like structure **III** has a similar donor atom count for the various Mn atoms, except that Mn(1) is now 6-coordinate through its adoption of a bridging interaction with the oxo bridge straddling Mn(3) and Mn(4). The necessity to maintain a 6-coordinate ligation of Mn(1) in **III**, but not in **I** is likely reflected in the observation that Mn(1) is promoted to the Mn^{IV} oxidation state in **III** as early as the +1 overall charge state, although this promotion in **I** does not occur until the +3 overall charge state. Formation of structure **III** is favoured when Mn(1) is in the +4 oxidation state, lacking a Jahn–Teller axis and thereby allowing effective sixfold coordination, whereas persistence of structure **I** as electrons are removed is favoured whereas Mn(1) remains in the +3 oxidation state, retaining a Jahn–Teller axis, which impedes close coordination of a sixth donor atom. The higher oxidation state on Mn(1) in **III** rather than in **I**, for the +1 and +2 oxidation states, is at the expense of Mn(4), which has an oxidation state of Mn^{III} for structure **I** in these charge states, but Mn^{II} for structure **III** in the same charge states. The lower charge state on Mn(4) in structure **III** is, in turn, facilitated by formation of the tri-μ-oxo bridge linking Mn(1) to Mn(4), because this tighter packing of the Mn atoms in **III** brings Mn(4) significantly closer to the Ca atom, ensuring that the (Asp170) ligand coordinated to Mn(4) employs its second O-donor atom in coordinating to Ca rather than chelating to Mn(4). This consequent imposition of coordinative unsaturation on Mn(4) in **III** favours the retention of a low oxidation state (+2) on this atom throughout the −1 to +2 charge states, whereas **I** exhibits promotion of Mn(4) from Mn^{II} to Mn^{III} as the overall charge state is increased from 0 to +1.

Interconversion of other forms with isomer **II** appears less facile, even when Mn atom oxidation states are similar (e.g. the 0 and +1 charge states of **I** and **II**). It is likely that interconversion between **II** and **III** would need to occur through a **I**-like intermediate, and in any case such an interconversion has not been seen in any of our calculations.

Preferred hydration sites: The positions of the three strongest-binding water ligands are not explicitly listed in the discussion above. It is, however, notable that the preferred water binding sites within the model are generally on Mn(4) or Ca. We also find that the water binding sites are only moderately influenced by the overall charge state and tend to be retained on ionization. It is also important to reiterate here that our reported results, for every charge state, consistently refer to *the lowest-energy trihydrated structure obtained by sequential removal of the least strongly bound water ligands from much more highly hydrated complexes* and, therefore, any "carry-over" of preferred hydration sites from one charge state to the next is not an artefact, but represents a genuine continued preference for these sites.

Structures $\mathbf{I}^{-1}$ and $\mathbf{I}^{0}$ adopt a tightly bound water ligand on Mn(4) which is retained through successive oxidations through to $\mathbf{I}^{+3}$, conveying at least tetrahedral coordination on this manganese atom; when Mn(4) is oxidised from Mn^{II} to Mn^{III} (in $\mathbf{I}^{+1}$ and subsequent charge states) a second water ligand attaches to this Mn. Structures $\mathbf{I}^{+2}$ and $\mathbf{I}^{+3}$, for which Mn(3) has been oxidised to Mn^{IV}, also feature a water ligand on Mn(3), conferring octahedral coordination on this

 © 2008 Wiley-VCH Verlag GmbH & Co. KGaA, Weinheim

metal atom (although in $\mathbf{I}^{+3}$, the Mn(3)-bound water ligand is in fact bridging between Mn(3) and Mn(4).

In structure **II**, only Mn(4) and the Ca atom are readily hydrated and only Ca^{II} is hydrated (in each case, doubly) in $\mathbf{II}^{-1}$ and $\mathbf{II}^{0}$ for which Mn(4) is identified as Mn^{II}. On promotion of Mn(4) to Mn^{III} (in $\mathbf{II}^{+1}$ and $\mathbf{II}^{+2}$), hydration occurs at this Mn atom (a second H_2O ligand is attached to Mn(4) abstracted from Ca^{II}) when this Mn atom attains the Mn^{IV} oxidation state in $\mathbf{II}^{+3}$.

In structure **III**, Mn(4) and Ca^{II} both feature a strongly bound water across all ionization states, to which is added a water ligand on Mn(3) in $\mathbf{III}^{+2}$ and $\mathbf{III}^{+3}$ when this Mn atom is in the Mn^{IV} oxidation state.

In all cases noted above, if the specified water ligand count falls below 3, the remaining water ligands within the lowest-energy trihydrated structure are nominally within the secondary coordination envelope of the metal atom; hydrogen bonded either to a carboxylate ligand, to a μ-oxo bridge, or to a primary-solvation-sphere water molecule.

Magnetic properties: The magnetic properties of **I**, **II** and **III** in their various charge states have been explored through calculations in which the spin polarization of each atom has been manipulated to explore a range of ferromagnetic and antiferromagnetic coupling patterns. Although only the purely ferromagnetic S_{max} state and the consistently antiferromagnetic ABAB configuration (in which Mn atoms 1 and 3 feature an α-spin electron excess; whereas the unpaired electrons on Mn atoms 2 and 4 are β-spin) are detailed in Table 3, separate geometry optimizations have been performed on all identifiable high-spin single-determinant configurations, as described in the Theoretical Methods section. The results of these calculations are detailed in tables provided in the supporting materials for this work and summarised in Figures 2, 3 and 4 for structures **I**, **II** and **III** respectively. The Supporting Information also provides a thorough discussion of magnetic-coupling trends across structure types and charge states. In general, antiferromagnetic coupling is energetically preferred over ferromagnetic, though by a progressively lower increment as the charge state is increased from −1 to +3.

Implications of the present results: Our results on structures ranging from the −1 to the +3 charge state (Figures 5 and 6) encompass several of the *S*-states assigned to the PSII water oxidation cycle, although there is currently no final consensus on the identity of the *S*-states. It is generally argued that the S_2 state is characterised by a Mn oxidation-state pattern of either $(Mn^{III})_3Mn^{IV}$ or $Mn^{III}(Mn^{IV})_3$. If the former possibility is adopted, our charge state distribution maps neatly onto the range of possible states from S_0 to S_4; if instead the latter interpretation applies, our −1 and 0 charge states do not correspond to any of the catalytic *S*-states, whereas the positively charged structures we have explored encompass S_0 to S_2. Note that all our efforts to characterise structures of charge state +4 or higher have been unsuccessful. This does not necessarily imply that the higher charge states are not feasible PSII *S*-states; rather, it is possible that the tendency to Coulombic explosion of highly charged species is responsible for their failure in our

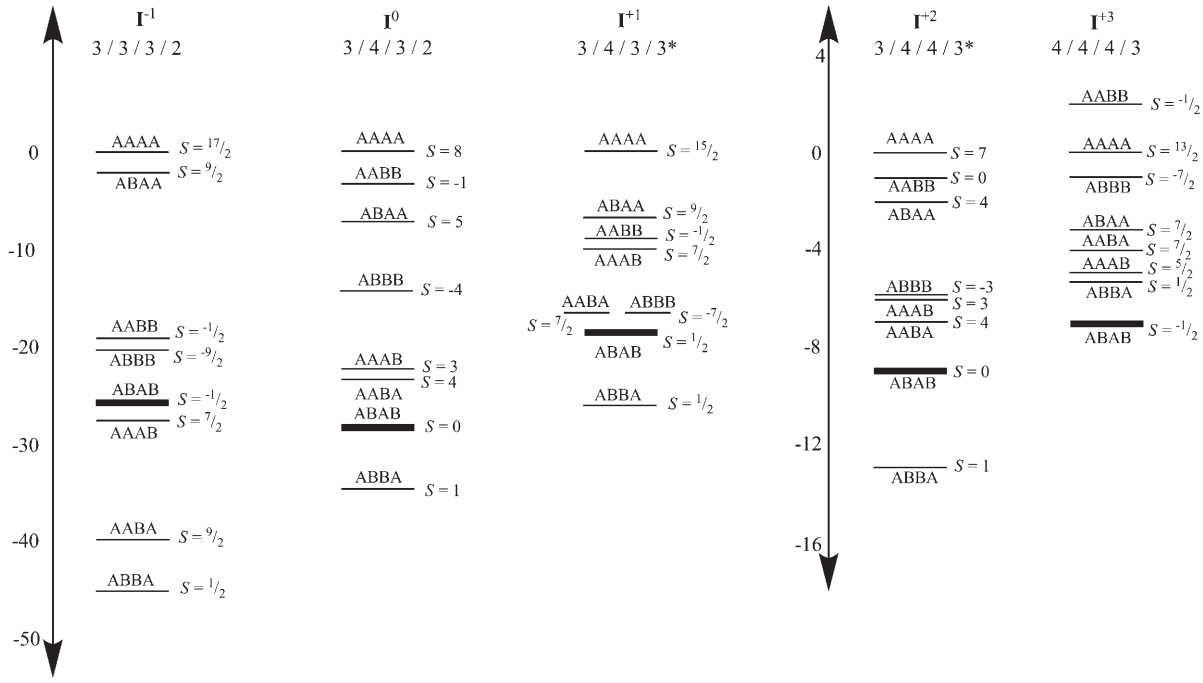

Figure 2. Energy diagram of all feasible high-spin single-determinant magnetic-coupling patterns for the Berlin-like structure $\mathbf{I}(H_2O)_3$ in five charge states. The A/B notation employed is as defined in the text. Energies are in kJ mol^{-1} and are expressed relative to the energy of the AAAA configuration in any given charge state.

 © 2008 Wiley-VCH Verlag GmbH & Co. KGaA, Weinheim

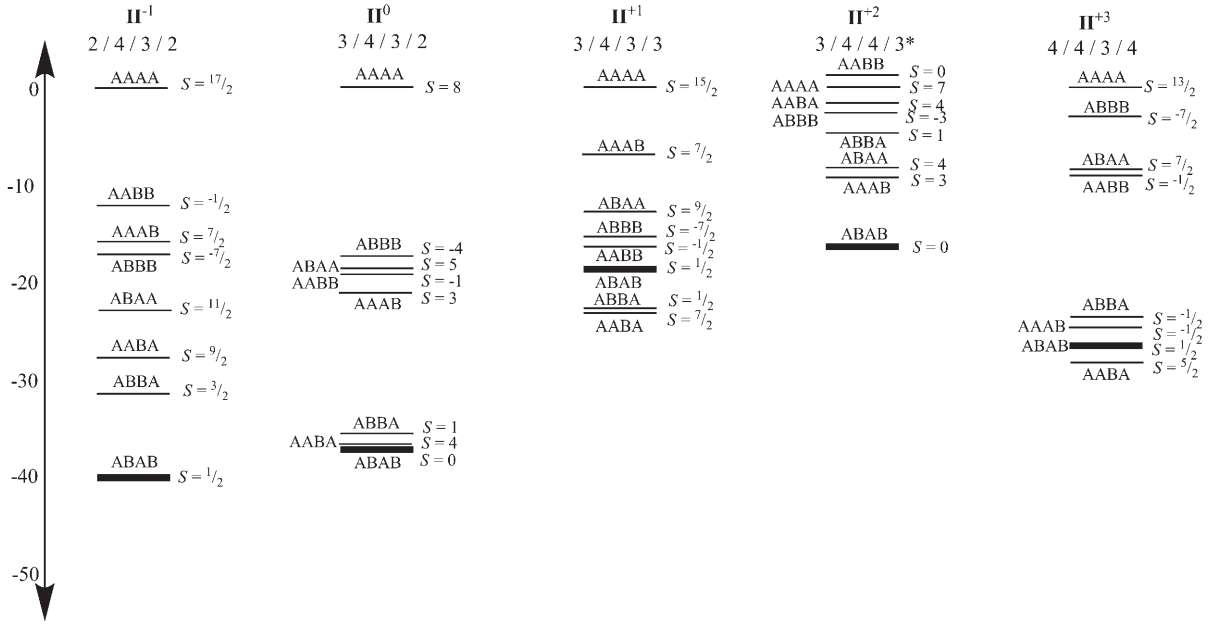

Figure 3. Energy diagram of all feasible high-spin single-determinant magnetic coupling patterns for the Hyogo-like structure $\mathbf{II}(H_2O)_3$ in five charge states. The A/B notation employed is as defined in the text. Energies are in kJ mol^{-1} and are expressed relative to the energy of the AAAA configuration in any given charge state.

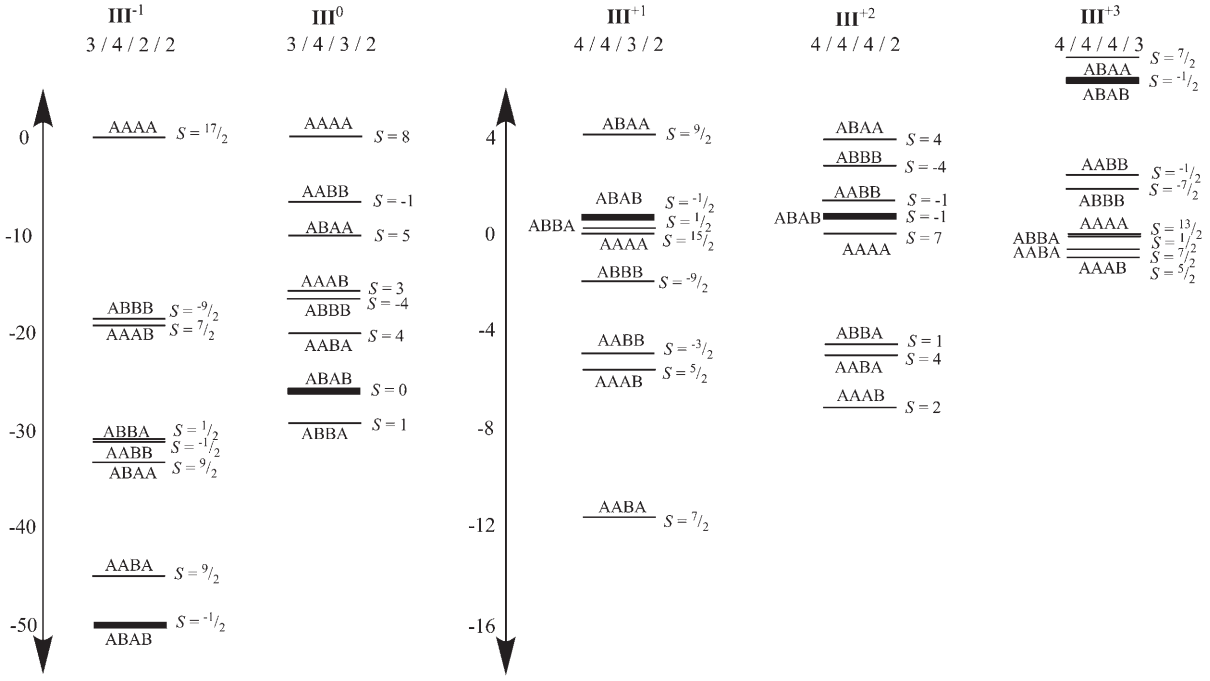

Figure 4. Energy diagram of all feasible high-spin single-determinant magnetic coupling patterns for the London-like structure $\mathbf{III}(H_2O)_3$ in five charge states. The A/B notation employed is as defined in the text. Energies are in kJ mol^{-1} and are expressed relative to the energy of the AAAA configuration in any given charge state.

vacuum-phase calculations. It should be noted that the theoretical models of the Siegbahn[7–9,11] and Batista[12–14] groups and of Kusunoki,[19] all feature geometries with significantly more anionic bridging ligands (O^{2-} and OH^-) than are incorporated in our models. This ensures that the models favoured by other groups exhibit greater stability at higher Mn oxidation states (e.g., the $Mn^{III}(Mn^{IV})_3$ interpretation of S_2) than do our models; conversely, a $Mn^{II}(Mn^{III})_3$ assignment for S_0 would imply, for more anionically bridged structures, a greater overall negative charge and consequent Coulombic

 © 2008 Wiley-VCH Verlag GmbH & Co. KGaA, Weinheim

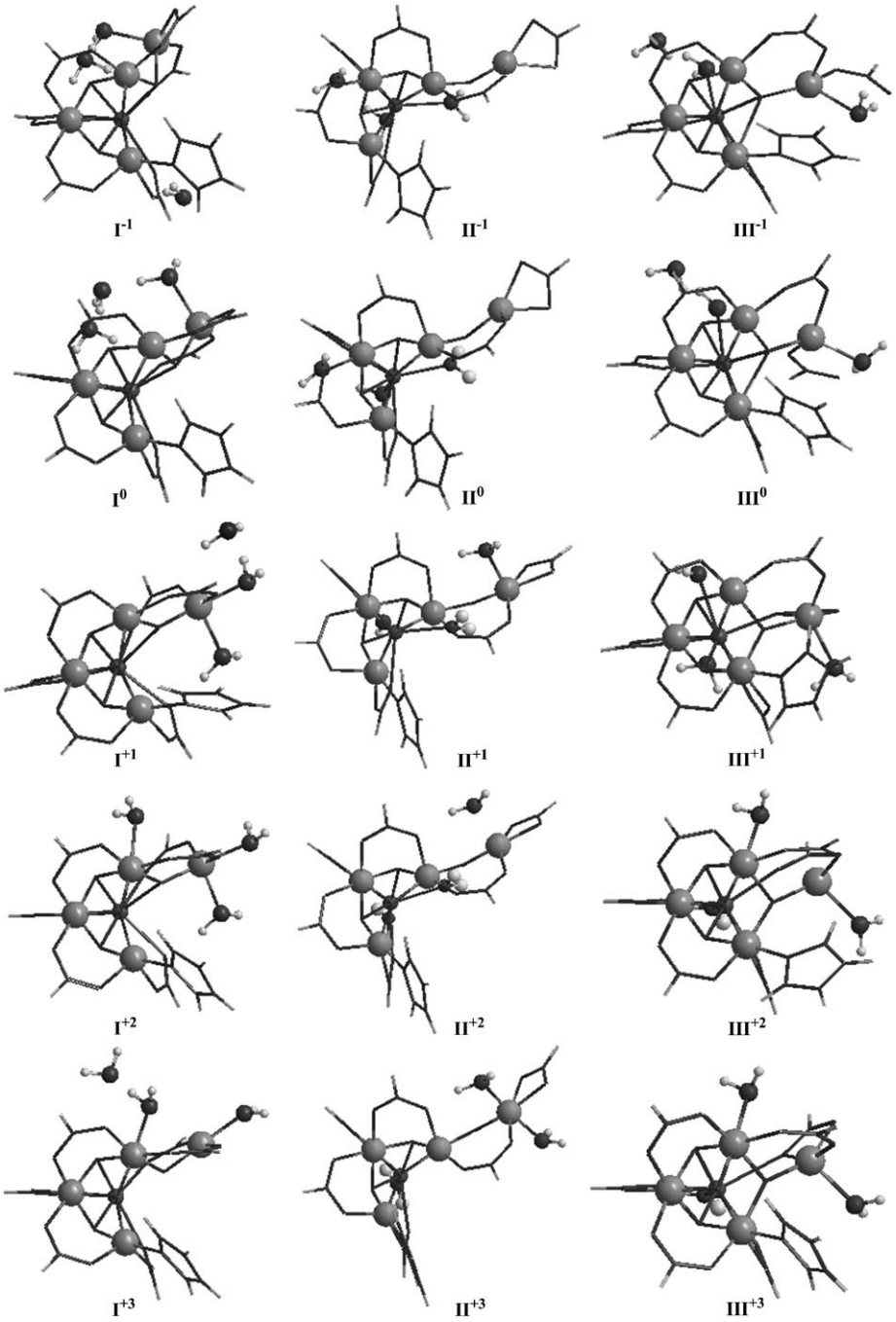

Figure 5. Optimized geometries of the triply-hydrated structures in all charge states at the BP/TZP level of theory (see Figure S1 in the Supporting Information for the red/blue stereographic projections).

instability in quantum chemical calculations. Although it is clearly highly desirable to characterise unambiguously the oxidation states for the sequence of PSII *S*-states, it is prudent in the absence of definitive information to remain open to both competing interpretations of the PSII oxidation state sequence. In the discussion that follows, we assume a $Mn^{II}(Mn^{III})_3$ oxidation state distribution for S_0, but caution that other interpretations exist (see below, Comparison with experimental data).

What implications do our results hold for understanding the mechanism of PSII water oxidation? We have previously commented that the energetic difference between structures **I**, **II** and **III** in the monopositive charge state is slight and insufficient to give a first-principles preference for any one architecture over the others. Given the similarities that these models have with the metal cores of respectively, the Berlin, Hyogo and London XRD structures, it is tempting to infer that the isolation of these divergent structures from the one initial source—that is, from PSII believed to be in the S_1 state—argues for a flexible and readily fluxional water oxidation site.

The results of our calculations on magnetic coupling (see also the Supporting Information) within the various charge states of **I**, **II** and **III** suggest, first, that Mn^{II} and Mn^{III} preferentially adopt a high-spin configuration in line with expectations. In general, antiferromagnetic coupling is preferred over ferromagnetic interactions; and it is also intriguing to note that, in both the $q=-1$ and $q=+2$ charge states, structures **II** and **III** both display considerable variability in the oxidation states of their constituent Mn atoms.

Interconversion between Berlin-like structure **I** and London-like structure **III** is particularly facile at the charge states $q=0$ and $q=+3$ in which both **I** and **III** have consistent Mn_4 oxidation-state patterns. At each of these charge states, the higher-energy structure (**III** at $q=0$, **I** at $q=+3$) is very susceptible to geometric distortion. Rearrangement of **III** to **I** is also comparatively facile at the $q=-1$ charge state. Further, it is interesting to note that the lowest-energy trihydrated structure at each charge state is **I** for $q=-1$ to $+2$ and **III** for $q=+3$. Thus, the minimum-energy cluster geometry is expected to be Berlin-like over the charge state range ($q=-1$ to $+2$), which is believed to model the S_0 to S_3 photo-states of the PSII WOC, but may adopt a London-like geometry within

 © 2008 Wiley-VCH Verlag GmbH & Co. KGaA, Weinheim

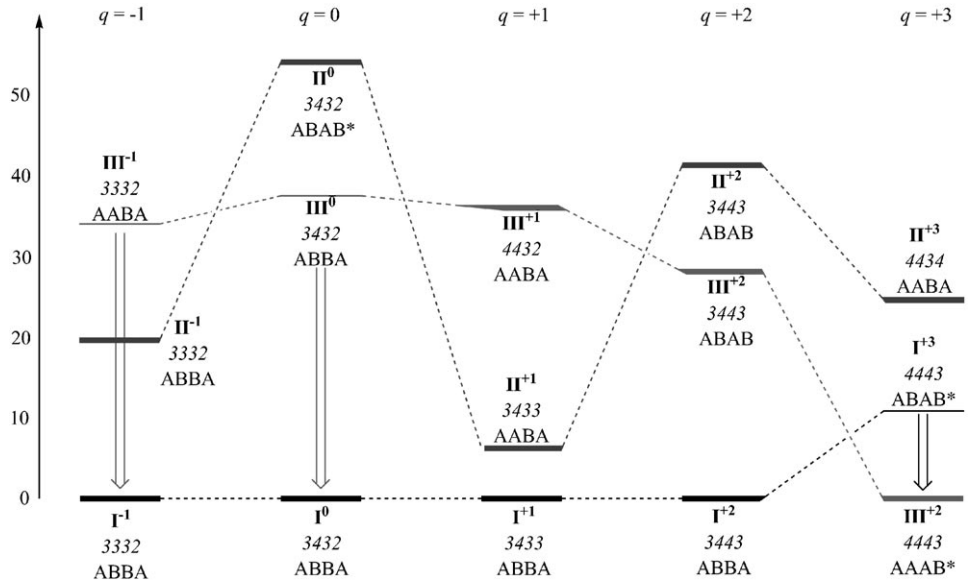

Figure 6. Schematic summary of oxidation state, geometry and magnetic coupling preferences as a function of cluster charge state. The structures of **I**, **II** and **III** are indicated. Structures not represented in bold are those considered prone to rearrangement to lower-energy geometries in the same charge state. The left-hand side axis indicates relative energies, in kJ mol^{-1}.

the transient S_4 state. This minimum energy oxidation sequence has several defining characteristics:

1) Assigning the $q=-1$ charge state as equivalent to S_0, this implies an S_0 configuration of $Mn^{III}Mn^{III}Mn^{III}Mn^{II}$ and an S_4 configuration of $Mn^{IV}Mn^{IV}Mn^{IV}Mn^{III}$. Thus each of the four Mn atoms is oxidised by one increment during the progression from S_0 to S_4. These oxidation steps are, in turn:
   $S_0 \rightarrow S_1$: Mn(2) is oxidised from Mn^{III} to Mn^{IV}
   $S_1 \rightarrow S_2$: Mn(4) is oxidised from Mn^{II} to Mn^{III}
   $S_2 \rightarrow S_3$: Mn(3) is oxidised from Mn^{III} to Mn^{IV}
   $S_3 \rightarrow S_4$: Mn(1) is oxidised from Mn^{III} to Mn^{IV}
2) Across all *S*-states, Mn(4) retains at least one strongly bound water ligand (two in the +1 and +2 charge states), with Mn(3) also picking up a water ligand in the +2 charge state (corresponding to S_3). Mn(1) and Mn(2) appear to lack strong water-binding sites.
3) ABBA is the lowest-energy single-determinant magnetic coupling pattern across the range of charge states (−1 to +2) which favour a Berlin-like structure, whereas London-like $\mathbf{III}^{+3}$ preferentially adopts an AAAB coupling pattern. The calculations suggest that antiferromagnetic coupling between Mn(1) and Mn(2) is preferred, as is the case also between Mn(3) and Mn(4), whereas the preferred mode of coupling between Mn(2) and Mn(3) is less clear-cut. (Although ABBA is generally lowest-energy, ABAB is often also comparatively low-energy). There is a consistent compression in the ladder of single-determinant magnetic-coupling configurations as the charge state is ramped from −1 to +3.
4) In the $q=+1$ charge state, the preferred geometry **I** is able to adopt either of two competing configurations. The $Mn^{III}Mn^{IV}Mn^{III}Mn^{III}$ (3433) configuration is about 40 kJ mol^{-1} lower in energy than $Mn^{III}Mn^{IV}Mn^{IV}Mn^{II}$ (3442) for this geometry. However the London-like geometry $\mathbf{III}^{+1}$, which is structurally related to $\mathbf{I}^{+1}$ by virtue of the ease of interconversion seen at other charge states, lies marginally lower in energy than the higher-energy (3442) of the two isolable $\mathbf{I}^{+1}$ configurations: $\mathbf{III}^{+1}$ has an oxidation-state pattern of $Mn^{IV}Mn^{IV}$-$Mn^{III}Mn^{II}$ (4432), different from either of the oxidation state distributions for $\mathbf{I}^{+1}$. Given the susceptibility of structures **I** and **III** for interconversion, the observation of these three distinct oxidation state distributions within a comparatively narrow energy range implies that the assigned oxidation states for Mn(1), Mn(3) and Mn(4) must all be regarded as malleable within this overall charge state: whereas each of Mn(1), Mn(3) and Mn(4) is nominally Mn^{III} in the lowest-energy configuration, Mn(1) and Mn(3) are also each capable of electron donation to Mn(4).

Similarly, in the +2 charge state, **I** preferentially adopts a $Mn^{III}Mn^{IV}Mn^{IV}Mn^{III}$ (3443) configuration, but a $Mn^{IV}Mn^{IV}Mn^{III}Mn^{III}$ (4433) configuration of $\mathbf{I}^{+2}$ lies about 40 kJ mol^{-1} higher, nearly isoenergetic with the $Mn^{IV}Mn^{IV}Mn^{IV}Mn^{II}$ (4442) configuration indicated by ferromagnetically coupled $\mathbf{III}^{+2}$ and slightly higher than the 3443 configuration preferred by some antiferromagnetically coupled variants of $\mathbf{III}^{+2}$ as detailed in a previous subsection. Again, strikingly, it is the Mn(1), Mn(3) and Mn(4) atoms that display variable oxidation states, whereas Mn(2) is apparently immutably locked in the Mn^{IV} oxidation state. The relevance of this oxidative uncertainty, in the context of the mechanism of water oxidation within PSII, is unclear, but we note that the invariant manganese, Mn(2), is the sole metal atom to exhibit the coordinative saturation of an octahedral ligand environment in the preferred structure **I**. It would therefore appear unlikely that Mn(2) is the site of water coordination and oxidation, for which one or more of the mutable oxidation state atoms Mn(1), Mn(3) or Mn(4) is a stronger candidate.

If, rather than a Berlin/London hybrid, the WOC geometry more closely corresponds to that of the Hyogo-like model **II**, a possibility that cannot be discounted on the basis of our vacuum-phase calculations, which though systematically favouring either **I** or **III** on energetic grounds in-

 © 2008 Wiley-VCH Verlag GmbH & Co. KGaA, Weinheim

dicate that structure **II** is never more than about 50 kJ mol^{-1} higher in energy than the lowest-energy structure at the same charge state, then the overall characteristics of this structure are rather different:

1) Assigning $q=-1$ as equivalent to S_0, implies an S_0 configuration of either $Mn^{III}Mn^{III}Mn^{III}Mn^{II}$ (lowest antiferromagnetic configuration) or $Mn^{II}Mn^{IV}Mn^{III}Mn^{II}$ (preferred ferromagnetic configuration) and an S_4 configuration of $Mn^{IV}Mn^{IV}Mn^{III}Mn^{IV}$. Here Mn(3) is never oxidised (although some transient Mn^{IV} character is attributed to it in $\mathbf{II}^{+2}$), Mn(4) is doubly oxidised and two oxidation steps occur among Mn(1) and Mn(2):
   $S_0 \rightarrow S_1$: Mn(1)Mn(2) is oxidised from either $Mn^{III}Mn^{III}$ or $Mn^{II}Mn^{IV}$ to $Mn^{III}Mn^{IV}$
   $S_1 \rightarrow S_2$: Mn(4) is oxidised from Mn^{II} to Mn^{III}
   $S_2 \rightarrow S_3$: Mn(1) is oxidised from Mn^{III} to Mn^{IV}
   $S_3 \rightarrow S_4$: Mn(4) is oxidised from Mn^{III} to Mn^{IV}
2) Unlike the Berlin/London hybrid, Mn(4) is not hydrated in the S_0 and S_1 states, in which it retains the Mn^{II} oxidation state and is chelated by Asp170 to give an approximately tetrahedral coordination that resists ready hydration. Instead, the favoured metal hydration site in these low *S*-states is the calcium atom (which in **II** is too distant to coordinate to either of the Asp170 carboxylate oxygen atoms and thus possesses a vacant O-donor coordination site). The calcium stays hydrated throughout the *S*-state cycle, whereas Mn(4) picks up a first water ligand for S_2 and S_3 and a second strongly bound water ligand for S_4.
3) No one magnetic coupling pattern is systematically preferred across the range of charge states surveyed here, although predominantly antiferromagnetic patterns (particularly, those antiferromagnetic between Mn(3) and Mn(4)) are generally lowest in energy. The preference for antiferromagnetic coupling generally drops, as the charge state q increases, although in sharp contrast to the Berlin/London hybrid, tricationic **II** is quite strongly antiferromagnetic.

Summarising these results, we find that the WOC geometry is robust with respect to the Mn_3Ca tetrahedron, which is not greatly influenced by repeated oxidation, but flexible in terms of the spatial relationship between Mn(4) and the other metal centres. A preference for antiferromagnetic coupling between Mn atoms is strongest in the S_0 state but remains significant up to S_3. Water ligation (and therefore, we presume, water oxidation) is most probable at Mn(4), but may also occur at Mn(3) and/or Ca depending upon the model geometry. Within most charge states, overall structural flexibility (in which Mn(4) is crucially implicated) and/or variability in the distribution of oxidation states across the four Mn atoms, must be considered as influences on the possible action of the WOC.

Comparison with experimental data: Ultimately, the computational results that we have obtained in the present study must be appraised in the light of extant experimental data on the WOC. In our earlier paper,[16] we compared the geometric properties of monocationic **I**, **II** and **III** to the various XRD structures of PSII[1,2,4,5] and to the most recently modelled EXAFS-derived structure.[20] Here we have investigated several charge states, which can conveniently be compared against the *S* state dependent XANES (X-ray absorption near-edge spectroscopy) and EXAFS data.[28–30]

Although the Mn oxidation state assignment for S_0 is debated, it is clear from the observed range of the S_0 edge position ($\approx$6550–6551 eV)[21] and other spectroscopic evidence[22] that the *functional* S_0 state contains no more than one Mn^{II}. Thus within the above possibilities, configurations such as $Mn^{II}Mn^{IV}Mn^{III}Mn^{II}$ are disfavoured for S_0. The situation for S_1 is less clear. All our calculations suggest a pattern of $Mn^{III}Mn^{IV}Mn^{III}Mn^{II}$ for this *S* state, whereas recent XANES edge shape interpretations would argue against the presence of Mn^{II}. However, there is a significant anomaly in the published XANES turnover data from several groups (as reviewed by Åhrling et al.).[21] These data fall into two sets, one which starts with an S_1 edge energy of $\approx$6553 eV and one with an edge energy $\approx$1.3 eV lower. The two sets are in much closer agreement for S_0. This observation has never been satisfactorily explained, but experimentally, S_0 is normally reached by flash turnover advancement from dark adapted S_1. One possibility is that the Mn oxidation states in S_1 are to some extent metastable, depending perhaps on details of sample preparation, cryoprotectant, etc. and that both $Mn^{III}Mn^{III}Mn^{III}Mn^{III}$ and $Mn^{III}Mn^{IV}Mn^{III}Mn^{II}$ are possible. Following passage through the catalytic transition, the system settles to its preferred functional state (presumably $Mn^{III}Mn^{III}Mn^{III}Mn^{III}$ in S_1). Recent EPR data make such an interpretation plausible.[23]

In Figure 7, we summarise the results of simulations of the recent *S* state dependent Mn EXAFS from Dau and coworkers.[24] The most detailed data fits from those authors

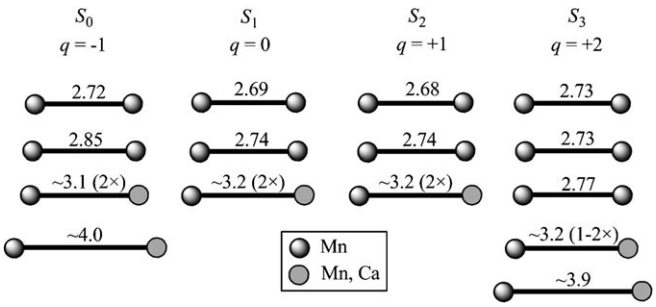

Figure 7. Summary of EXAFS-derived metal–metal distance values from the study of Dau and co-workers.[30]

are shown.[24] We also indicate approximate interpretations of the distant scatterer peaks resolved in S_0 and S_3, which were not analysed in the original paper.[30] If the EXAFS-derived metal–metal distances are compared with the geometries reported in Table 1, the fit is somewhat better for the scenario in which S_0 is $Mn^{II}(Mn^{III})_3$, or equivalent (i.e. $q=$

 © 2008 Wiley-VCH Verlag GmbH & Co. KGaA, Weinheim

−1), than for the case in which S_0 is $(Mn^{III})_3Mn^{IV}$ or equivalent (i.e. $q=+1$). For example, all of the $q=-1$ structures have at least one Mn−Mn distance in the required 2.8–2.9 Å range (though the lowest-energy $q=-1$ structure, $\mathbf{I}^{-1}$ probably has too many short Mn−Mn distances to match the EXAFS data), whereas none of the $q=+1$ structures have any Mn−Mn separations in this distance range. However, regardless of the S_0 oxidation-state pattern, there are several structural assignments, which hold true for all $q=-1$ and $q=+1$ structures. First, the two short Mn−Mn distances seen for S_0 are identifiable as Mn(1)−Mn(2) and Mn(2)−Mn(3). Second, the features seen at 3.1–3.2 Å are most probably Mn(3)−Mn(4) and Mn(2)−Ca. Third, the ≈4 Å EXAFS feature apparent in S_0 and S_3 is presumed to include some Mn−Ca contribution because insufficient Mn−Mn vectors of this magnitude occur within any structure.

Also in the EXAFS data, the most pronounced change in the second coordination sphere Mn−Mn pattern occurs on the $S_2\rightarrow S_3$ transition. Although the precise interpretation of this change is disputed,[24–26] it has been most recently modelled[24] as the emergence of an additional short (≈2.7 Å) Mn−Mn distance at S_3. This change is broadly consistent with the contraction in the Mn(1)−Mn(3) distance in structure **III** for the cationic charge states. In our calculations this occurs between $q=0$ and $q=+1$ (i.e., across the putative $S_1\rightarrow S_2$ transition), but could occur on $S_2\rightarrow S_3$ if the S_2 geometry were significantly different than $\mathbf{III}^{+1}$, yielding $\mathbf{III}^{+2}$ on oxidation. The best overall match between our results and the EXAFS data appears to be $\mathbf{II}^{-1}$ for S_0 (which shows good agreement with the short Mn−Mn distances and, uniquely, has several near-identical metal–metal separations near 3.7 Å, generally consistent with the S_0 scatter peak mentioned above), $\mathbf{II}^{0}$ for S_1 (again, a good fit with the short Mn−Mn distances, in both length and number of such interactions), $\mathbf{II}^{+1}$ for S_2 (inferior to $\mathbf{III}^{+1}$ in terms of agreement with the two shortest Mn−Mn separations, but $\mathbf{III}^{+1}$ arguably has too many such interactions; $\mathbf{II}^{+1}$ also does a better job of matching the 3.2 Å feature seen in the EXAFS data) and $\mathbf{III}^{+2}$ for S_3. It should be acknowledged, however, that the calculations reported here deal only with the pure hydrated clusters and do not explore the influence of deprotonation which almost certainly accompanies oxidation within some steps of the WOC oxygen-generation mechanism.

Theoretical methods: Density functional theory calculations employed the Amsterdam Density Functional (ADF) program, version ADF 2004.01, developed by Baerends et al.[27–29] Calculations were run in parallel mode on the AlphaSever supercomputer housed at the ANU Supercomputer Facility and operated under the Australian Partnership for Advanced Computing.

Geometry optimizations, in C_1 symmetry, used the gradient algorithm of Versluis and Ziegler[30] and featured convergence constraints twice as tight as the ADF default values. Electrons in orbitals up to and including 1s {C, N, O} or 2p {Mn} were treated in accordance with the frozen-core approximation. All calculations were performed in an unrestricted fashion.

In our preliminary investigation of the $[CaMn_4C_9H_{10}N_2O_{16}]^{q+}\cdot(H_2O)_i$ potential energy surface ($q=-1$, 0, 1, 2, 3), ($i=0$–7), optimizations were performed in the fully ferromagnetically coupled, all-high-spin $S_{max}=(16-q)/2$ spin state. Optimized S_{max} geometries were then reoptimised in a broken symmetry (BS) configuration[31] with the spin polarization on sequential Mn atoms as αβαβ (hereafter ABAB). This configuration has $|M_S|=(0, \frac{1}{2}, \text{or } 1)$ depending on the oxidation states of the respective Mn atoms. These calculations were employed to determine the preferred sites of hydration for $[CaMn_4C_9H_{10}N_2O_{16}]^{q+}\cdot(H_2O)_3$ as follows. The heptahydrated structure $[CaMn_4C_9H_{10}N_2O_{16}]^{q+}\cdot(H_2O)_7$ was characterized and the fully dehydrated $[CaMn_4C_9H_{10}N_2O_{16}]^{q+}$ geometry from this calculation was then itself optimized. Then, individual water molecules at the positions determined from the $[CaMn_4C_9H_{10}N_2O_{16}]^{q+}\cdot(H_2O)_7$ calculation were added to the optimized $[CaMn_4C_9H_{10}N_2O_{16}]^{q+}$ structure; these monohydrated structures were themselves optimized and a determination of the next preferred water binding site at each hydration level was built up incrementally. This lengthy computational strategy was judged the most appropriate method by which to ensure that the most stable $[CaMn_4C_9H_{10}N_2O_{16}]^{q+}\cdot(H_2O)_3$ structures could be characterized at each charge state. Note that here, we report only the results obtained for $[CaMn_4C_9H_{10}N_2O_{16}]^{q+}\cdot(H_2O)_3$; a detailed description of the revealed hydration trends is beyond the scope of the present work and will be published separately.

Following identification of the lowest-energy $[CaMn_4C_9H_{10}N_2O_{16}]^{q+}\cdot(H_2O)_3$ ($q=-1$, 0, 1, 2, 3) structures, the geometry optimized for the ABAB broken symmetry configuration was used in further optimizations on each of the six other feasible non-equivalent single-determinant broken-symmetry, all-high-spin electronic configurations. These six configurations can be denoted respectively as AAAB, AABA, ABAA, AABB, ABBA and ABBB. Additionally, for each Mn^{III}-containing structure a geometry optimization with AAAA coupling was sought for $S_{max}=(14-q)/2$, representing a fully ferromagnetic structure in which one Mn^{III} was low-spin; similarly, in structures possessing one or more Mn^{II} atoms AAAA coupling was also investigated for the low-spin Mn^{II} scenario with $S_{max}=(12-q)/2$. We did not explore structures featuring two or more low-spin Mn atoms, on the expectation that such structures would be strongly disfavoured on energetic grounds.

Functionals used in the calculations were the local density approximation (LDA) to the exchange potential, the correlation potential of Vosko, Wilk and Nusair (VWN),[32] and the nonlocal corrections of Becke[33] and Perdew.[34] The (Slater type orbital) basis sets used were of triple-ζ-plus-polarization quality (TZP).

 © 2008 Wiley-VCH Verlag GmbH & Co. KGaA, Weinheim

Conclusion

The candidate PSII WOC models **I**, **II** and **III** have been explored in overall charge states -1 to $+3$ and in all feasible single-determinant high-spin magnetic coupling configurations. Extending our previous study of the $+1$ charge state, we find that structures **I** and **III** very readily interconvert: **III** to **I** in the $q=-1$ and 0 charge states and **I** to **III** in the $q=+3$ charge state. In contrast, **II** maintains a more distinct identity in all surveyed charge states. The preferred magnetic coupling is predominantly antiferromagnetic, particularly in the -1 and 0 charge states; at the highest charge states for structures **I** and **III**, there is little energetic difference between fully ferromagnetically coupled and consistently antiferromagnetically coupled configurations.

Within each charge state the structures are energetically close considering the size of the systems examined. The energy difference is never greater than about $50\,kJ\,mol^{-1}$, barely the energy of two hydrogen bonds. This strongly suggests that the calculated energy rankings in vacuo might be readily altered in the protein environment. Thus, although structure **I** is favoured energetically, comparisons with the EXAFS derived experimental metal–metal distances gives preference to a model in which structure **II** is maintained throughout the earlier S states (S_0 to S_2) then a transition occurs to another structural type in S_3 which is more compact with closer average Mn–Mn distances. It is interesting in this regard, that the computations generally suggest that structure **II** is more resistant to interconversion, as noted above and that a significant geometric change occurs only in S_3 when the catalytic stage is set.

Among the metal atoms of the $CaMn_4$ cluster, the location of Mn(4) is uniquely variable, both as a function of charge state and across the three structural motifs **I** to **III**, which we have explored here. This positional flexibility contrasts with the robust near-invariance of the distorted tetrahedron comprising Mn(1), Mn(2), Mn(3) and Ca, which withstands disruption across structural types and over the range of charge states $q=-1$ to $+3$.

Within several of the charge states explored here, the oxidation states on Mn(1), Mn(3) and Mn(4) differ between models **I**, **II** and **III**. These differences can be rationalised in terms of minor differences in ligation: chelation of the Asp170 carboxylate group by Mn(4) in **II**, versus a bridging interaction by this carboxylate between Mn(4) and Ca in **I** and **III**; and the formation of a second tri-μ-oxo bridge, linking Mn(1) to Mn(3) and Mn(4), present in **III** but absent in **I** and **II**. The sensitivity of the respective oxidation states to these subtle ligation effects may well be relevant to the biochemical function of PSII, in the same manner as the WOC's apparent structural flexibility.

Acknowledgements

R.S. and R.J.P. gratefully acknowledge financial assistance from the Australian Research Council. The authors also acknowledge the generous provision of supercomputing time on the platforms of the Australian Partnership for Advanced Computing, operating through the Australian National University Supercomputing Facility.

[1] A. Zouni, H.-T. Witt, J. Kern, P. Fromme, N. Krauss, W. Saenger, P. Orth, *Nature* **2001**, *409*, 739–743.
[2] N. Kamiya, J.-R. Shen, *Proc. Natl. Acad. Sci. USA* **2003**, *100*, 98–103.
[3] J. Biesiadka, B. Loll, J. Kern, K.-D. Irrgang, A. Zouni, *Phys. Chem. Chem. Phys.* **2004**, *6*, 4733–4736.
[4] K. N. Ferreira, T. M. Iverson, K. Maghlaoui, J. Barber, S. Iwata, *Science* **2004**, *303*, 1831–1838.
[5] B. Loll, J. Kern, W. Saenger, A. Zouni, J. Biesiadka, *Nature* **2005**, *438*, 1040–1044.
[6] J. Yano, J. Kern, K.-D. Irrgang, M. J. Latimer, U. Bergmann, P. Glatzel, Y. Pushkar, J. Biesiadka, B. Loll, K. Sauer, J. Messinger, A. Zouni, V. K. Yachandra, *Proc. Natl. Acad. Sci. USA* **2005**, *102*, 12047–12052.
[7] P. E. M. Siegbahn, *Q. Rev. Biophys.* **2003**, *36*, 91–145.
[8] M. Lundberg, P. E. M. Siegbahn, *Phys. Chem. Chem. Phys.* **2004**, *6*, 4772–4780.
[9] P. E. M. Siegbahn, M. Lundberg, *Photochem. Photobiol. Sci.* **2005**, *4*, 1035–1043.
[10] P. E. M. Siegbahn, M. R. A. Blomberg, *Philos. Trans. R. Soc. A* **2005**, *363*, 847–860.
[11] P. E. M. Siegbahn, M. Lundberg, *J. Inorg. Biochem.* **2006**, *100*, 1035–1040.
[12] J. P. McEvoy, J. A. Gascon, V. S. Batista, G. W. Brudvig, *Photochem. Photobiol. Sci.* **2005**, *4*, 940–949.
[13] E. M. Sproviero, J. A. Gascon, J. P. McEvoy, G. W. Brudvig, V. S. Batista, *J. Inorg. Biochem.* **2006**, *100*, 786–800.
[14] E. M. Sproviero, J. A. Gascon, J. P. McEvoy, G. W. Brudvig, V. S. Batista, *J. Chem. Theory Comput.* **2006**, *2*, 1119–1134.
[15] M. Kusunoki, *Biochim. Biophys. Acta Bioenerg.* **2007**, *1767*, 484.
[16] S. Petrie, R. Stranger, P. Gatt, R. J. Pace, *Chem. Eur. J.* **2007**, *13*, 5082.
[17] K. A. Åhrling, M. C. W. Evans, J. H. A. Nugent, R. J. Ball, R. J. Pace, *Biochemistry.* **2006**, *45*, 7069–7082.
[18] Note that the preferred antiferromagnetic coupling pattern is not always ABAB, according to our calculations; however, within a given oxidation-state pattern the variance between differently coupled optimized geometries is generally rather slight. More dramatic geometric differences can arise can arise when antiferromagnetically coupled structures have an oxidation-state pattern, which differs from that dictated by ferromagnetic coupling, as is the case for example for $\mathbf{II}^{-1}$ and $\mathbf{III}^{+2}$ (discussed subsequently within the text). The geometry relevant to the ferromagnetically coupled oxidation-state pattern, as shown in Table 1 is, however, likely to be more useful as a comparison with experimental structural data obtained from flash turnover conducted at, or near, room temperature.
[19] M. Kusonoki, *Biochim. Biophys. Acta Bioenerg.* **2007**, *1767*, 484.
[20] J. Yano, J. Kern, K. Sauer, M. J. Latimer, Y. Pushkar, J. Biesiadka, B. Loll, W. Saenger, J. Messinger, A. Zouni, V. K. Yachandra, *Science* **2006**, *314*, 821.
[21] K. A. Åhrling, R. J. Pace, M. C. W. Evans in *Photosystem II—The Light-Driven Water:Plastoquinone Oxidoreductase*, (Eds.: T. J. Wydrzynski, K. Satoh), Springer, Dordrecht, the Netherlands, **2005**, pp. 285–305.
[22] D. Kuzek, R. J. Pace, *Biochim. Biophys. Acta Bioenerg.* **2001**, *1503*, 123–137.
[23] S. Peterson, K. A. Åhrling, J. E. P. Högblom, *Biochemistry* **2003**, *42*, 2748–2758.
[24] M. Haumann, C. Müller, P. Liebisch, L. Iuzzolino, J. Dittmer, M. Grabolle, T. Neisius, W. Meyer-Klaucke, H. Dau, *Biochemistry* **2005**, *44*, 1894–1908.
[25] H. Visser, E. Anxolabehere-Mallart, U. Bergmann, P. Glatzel, J. H. Robblee, S. P. Cramer, J.-J. Girerd, K. Sauer, M. P. Klein, V. K. Yachandra, *J. Am. Chem. Soc.* **2001**, *123*, 7031–7039.

 © 2008 Wiley-VCH Verlag GmbH & Co. KGaA, Weinheim

[26] W. Liang, T. A. Roelofs, R. M. Cinco, A. Rompel, M. J. Latimer, W. O. Yu, K. Sauer, M. P. Klein, V. K. Yachandra, *J. Am. Chem. Soc.* **2000**, *122*, 3399–3412.
[27] C. F. Fonseca Guerra, J. G. Snijders, G. te Velde, E. J. Baerends, *Theor. Chem. Acc.* **1998**, *99*, 391–403.
[28] G. te Velde, F. M. Bickelhaupt, E. J. Baerends, C. F. Guerra, S. J. A. van Gisbergen, J. G. Snijders, T. Ziegler, *J. Comput. Chem.* **2001**, *22*, 931–967.
[29] E. J. Baerends, J. Autsbach, A. Bérces, C. Bo, P. M. Boerrigter, L. Cavallo, D. P. Chong, L. Deng, R. M. Dickson, D. E. Ellis, L. Fan, T. H. Fischer, C. Fonseca Guerra, S. J. A. van Gisbergen, J. A. Groeneveld, O. V. Gritsenko, M. Gruning, F. E. Harris, P. van den Hoek, H. Jacobsen, G. van Kessel, F. Kootstra, E. van Lenthe, D. A. McCormack, V. P. Osinga, S. Patchkovskii, P. H. T. Philipsen, D. Post, C. Pye, W. Ravenek, P. Ros, P. R. T. Schipper, G. Schreckenbach, J. G. Snijders, M. Sola, M. Swart, D. Swerhone, G. te Velde, P. Vernooijs, L. Versluis, O. Visser, E. van Wezenbeek, G. Wiesenekker, S. K. Wolff, T. K. Woo, T. Ziegler, *Amsterdam Density Functional*, version 2004.01, Theoretical Chemistry, Vrije Universiteit, Amsterdam, the Netherlands, http://www.scm.com, **2004**.
[30] L. Versluis, T. Ziegler, *J. Chem. Phys.* **1988**, *88*, 322–328.
[31] L. Noodleman, *J. Chem. Phys.* **1981**, *74*, 5737–5743.
[32] S. H. Vosko, L. Wilk, M. Nusair, *Can. J. Phys.* **1980**, *58*, 1200.
[33] A. D. Becke, *Phys. Rev. A* **1988**, *38*, 3098–3100.
[34] J. P. Perdew, *Phys. Rev. B* **1986**, *33*, 8822.

Received: November 27, 2007
Published online: May 9, 2008

 © 2008 Wiley-VCH Verlag GmbH & Co. KGaA, Weinheim